AIAA JOURNAL
Vol. 30, No. 4, April 1992

Calculation of Real-Gas Effects on Blunt-Body Trim Angles

Chul Park*
NASA Ames Research Center, Moffett Field, California 94035
and
Seokkwan Yoon†
MCAT Institute, Moffett Field, California 94035

The effect of vibrational excitation and dissociation at high temperatures on the trim angle of attack of a blunt lifting body is calculated for a nonequilibrium flow regime in air using a computational fluid dynamics technique. Air is considered to consist of five neutral species, O, N, NO, O_2, and N_2, and both one- and two-temperature thermochemical nonequilibrium models are used in determining the thermodynamic state. A computer code, named CENS2H (Compressible Euler-Navier-Stokes Two-dimensional Hypersonic), is developed by incorporating this model into an existing perfect-gas code named CENS2D, which uses a lower-upper factorization based on the symmetric Gauss-Seidel sweeping technique. The code is applied to compute the forebody flow of a two-dimensional blunt body of the shape of the Apollo Command Module at a finite angle of attack. The results show that the trim angle of attack is smaller for a reacting gas than for a perfect gas. The calculated shift in the trim angle due to the real-gas effect is of the same order as that seen during the Apollo flights. The one-temperature nonequilibrium model yields the same trim angles as the two-temperature model, but the constant-γ ($= C_p/C_v$) solution that reproduces the shock standoff distance fails to reproduce the trim angle.

Nomenclature

A = Jacobian of the x or ξ component of the inviscid flux
$\mathbf{A}$ = first parameter in the Millikan and White's formula, Eq. (1)
a_i = coefficients in equilibrium-constant expression, Eq. (7)
a/a = angle of attack
B = Jacobian of the y or η component of the inviscid flux
$\mathbf{B}$ = second parameter in the Millikan and White's formula, Eq. (1)
C = rate constant, m^3 $mole^{-1}$ s^{-1}
C_D = drag coefficient
C_L = lift coefficient
C_m = pitching moment coefficient around the reference point
C_p = pressure coefficient
D_η = difference operator along η
D_ξ = difference operator along ξ
d = body diameter, m
E = energy per unit volume, J/m^3
E_e = electronic excitation energy per unit volume, J/m^3
E_v = vibrational energy per unit volume, J/m^3
e = vertical c.g. offset, m
F = x or ξ component of the inviscid flux
F_v = x or ξ component of the viscous flux
G = y or η component of the inviscid flux
G_v = y or η component of the viscous flux
H = Jacobian of the thermochemical source S
I = unit matrix
K_e = equilibrium constant
k_f = forward (endothermic) reaction rate coefficient
k_r = reverse (exothermic) reaction rate coefficient
n = pre-exponential power on temperature in rate coefficient, Eq. (6)
n_i = number density of species i, mole/m^3
p = pressure, Pa or atm
Q = conserved variable
R = right-hand-side residual
S = thermochemical source term
s = exponent used in bridging between Landau-Teller and diffusion formulas, Eq. (3)
T = translational-rotational temperature, K
T_a = average temperature
T_d = characteristic temperature of reaction, K, Eq. (6)
T_v = vibrational-electronic temperature, K
t = time
u = x or ξ component of velocity
v = y or η component of velocity
W_e = strength of the chemical source for electronic energy, J/(m^3 s)
W_i = strength of chemical source of species i, kg/(m^3 s)
W_v = strength of chemical source for vibrational energy, J/(m^3 s)
w_{ij} = rate of change of vibration energy of species i by the collisions of species, j, J/(mole-s)
x = horizontal coordinate, m
$\bar{x}$ = x coordinate of center of gravity, m
x_{mc} = distance from stagnation point to the metacenter, m
y = vertical coordinate, m
α = angle of attack, deg
α_t = trim angle of attack, deg
γ = specific heat ratio in perfect gas
ϵ_{ei} = electronic excitation energy of species i, J/mole
η = curvilinear coordinate normal to body surface
ξ = curvilinear coordinate along body surface
ρ = density, kg/m^3
ρ_i = density of species i, kg/m^3

Presented as Paper 89-0685 at the AIAA 27th Aerospace Sciences Meeting, Reno, NV, Jan. 6–9, 1989; received March 3, 1989; revision received April 6, 1991; accepted for publication May 16, 1991.

*Head, Experimental Aerothermodynamics Section. Associate Fellow AIAA.

†Senior Scientist. Member AIAA.

τ_c = elastic collision time
τ_L = vibrational relaxation time in Landau-Teller expression given by Eq. (1)

Subscripts
c = elastic collisions
L = Landau-Teller model
r = thermochemical processes
s = shock wave

Introduction

SPURRED by the advances made in the space transportation technology, efforts have begun in recent years to compute the hypersonic flowfields around re-entry vehicles including the thermochemical real-gas effects at the high temperatures occurring within the shock layer (see, e.g., Ref. 1). The efforts have been made to determine the effects of atomic oxygen on the convective heat transfer rates on the catalytic and noncatalytic walls, to determine the electron densities in the shock layer,[2] and to calculate the radiative heat transfer rates.[3]

There remains one aspect of the high-temperature real-gas effects that has not yet been addressed, namely, the problem of its effects on the aerodynamic characteristics of the hypersonic vehicles. The rise in density due to the real-gas effects causes the shock layers around a hypersonic vehicle to be thinner than in a perfect gas. A thinner shock layer causes the shock angle to be smaller than in the perfect-gas case. This leads to a change in pressure distribution over the airframe,[1] resulting in changes in lift, drag, and pitching moment. The change in the pitching moment causes the trim angle of attack to change. As the trim angle changes, the lift and drag at the trim point also change, causing the flight path of the vehicle to change.

During the entry flights of both Apollo[4,5] and Space Shuttle[6] vehicles, the trim angle of attack changed appreciably in the high Mach number (above 10) regime: a positive (nose-up) pitching moment has developed. In Figs. 1a and 1b, the geometry of the Apollo Command Module[5] is shown. As Fig. 1a shows, the center of gravity, c.g., of the Apollo vehicle was offset slightly from the centerline axis. Because of this c.g. offset, the vehicle trimmed at a finite angle of attack. The angle of attack was defined for the Apollo vehicle from the apex of the body, as shown in Fig. 1a. Through the tests in wind tunnels, which produced perfect-gas flows, the trim angle of attack was determined as a function of the c.g. location. According to the prediction, the vehicle should have trimmed at an angle of attack α_t between 151 and 159 deg, the exact angle being different for each flight because the c.g. location was different for each flight. The trim angles for the first three of the Apollo flights (flights AS-202, Apollo 4, and Apollo 6) are given in Refs. 4 and 5. The flight data showed that α_t was generally larger than predicted; that is, the vehicles flew at more nose-up attitudes, producing less lift. Figure 2 shows the difference between the measured trim angles of attack and those predicted from the wind-tunnel tests, $\Delta\alpha_t$. As seen in the figure, $\Delta\alpha_t$ was about 2 deg on the average in the hypersonic flight range, reaching as much as 4 deg at a Mach number of 30.

A nose-up pitching moment was produced also during the entry flights of the Space Shuttle Orbiter; that is, the center of pressure moved forward. The forward shift in the center of pressure was consistent and reproducible and was larger at larger Mach numbers.[6]

Several investigators considered the shift in the trim angle to be caused by the high-temperature real-gas effects that would be present in flight but not in the cold wind-tunnel flow.[4-8] Others considered it to be caused by the low-density viscous effects[9] or by ablation.[10]

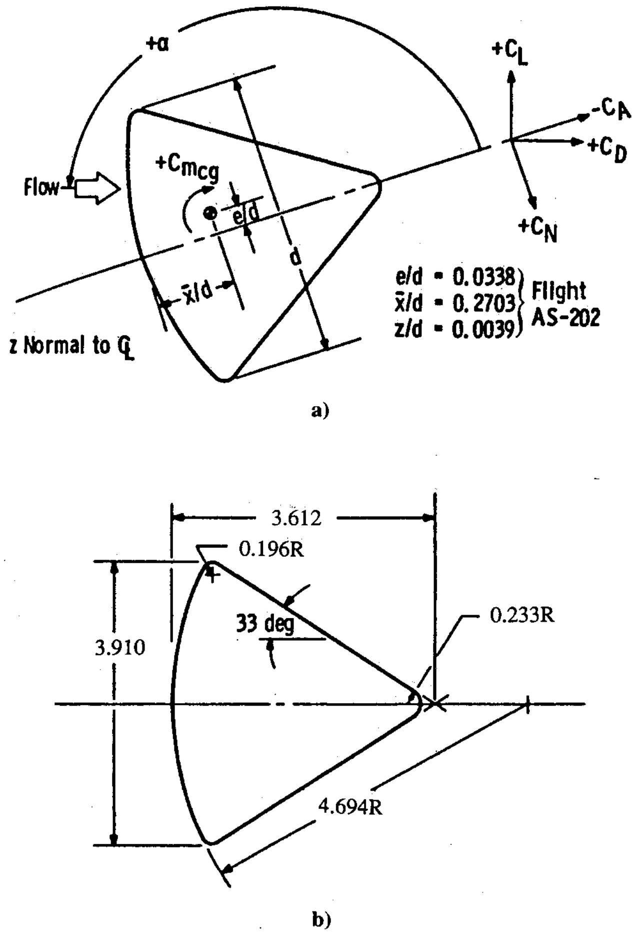

a)

b)

Fig. 1 Geometry of the Apollo vehicle AS-202: a) center of gravity; b) dimensions.

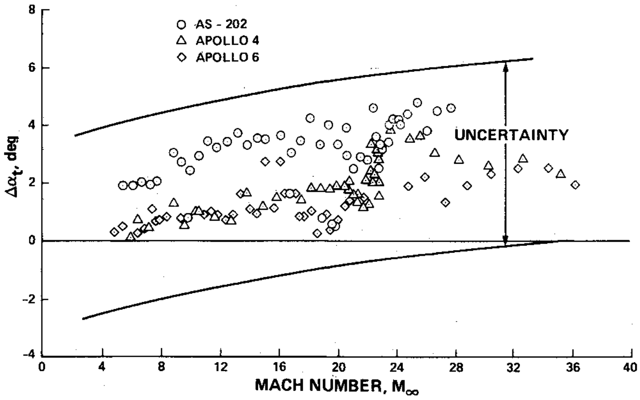

Fig. 2 Difference between the trim angles of attack during the flights of AS-202, Apollo 4, and Apollo 6 and those predicted from the wind-tunnel tests.

The trim angle of attack is an important aerodynamic parameter not only for the Apollo and Space Shuttle vehicles, but also for all future hypersonic vehicles. For this reason, it is highly desirable to be able to determine it computationally. It is the purpose of the present work to explore whether such a computation is feasible. In order to start with a relatively simple problem, we limit our considerations to the suborbital flight speeds, that is, speeds below about 8 km/s.

For this purpose, we have developed a new computer code by combining an existing nonequilibrium thermochemical (two-temperature) model with an existing perfect-gas computer code named CENS2D (Compressible Euler-Navier-Stokes Two-Dimensional).[11,12] The basic method of coupling thermochemistry with the fluid motion is the same as in the work of Shuen and Yoon.[13] The resulting code, named tentatively CENS2H where H signifies Hypersonic, is applied to a flow around a two-dimensional body with the same profile as that of the Apollo Command Module. The solutions are obtained for the forebody shock layer of this body. The lift, drag, and pitching moment, and trim angle of attack are calculated from the pressure distribution obtained from the computation. The results show that the trim angle of attack changes due to the high-temperature real-gas effects. The magnitude of the shift in the trim angle is of the same order as that observed during the flights of the Apollo vehicles. Trim angles are calculated also with the conventional thermal-equilibrium, chemical-nonequilibrium (one-temperature) model and the perfect-gas model, and the results are compared with the thermochemical nonequilibrium calculations.

Method of Calculation

Thermochemical Model

General Remarks

The high-temperature real-gas effects are calculated in the present work using the two-temperature model developed in Refs. 3, 14, and 15. According to the model, we assume that the rotational mode is in equilibrium with the translational mode and that the two modes are characterized by the translational-rotational temperature T. We assume also that the electronic excitation mode is in equilibrium with the vibrational mode and that the two modes are characterized by the vibrational-electronic temperature T_v. All three molecules, O_2, N_2, and NO, are assumed to be at the same vibrational temperature. The justification for the last assumption is given later.

In the suborbital flight-speed range, the only significant ionization process is the associative ionization

$$N + O \rightarrow NO^+ + e - 2.8\ \text{eV}$$

The process transfers heavy particle translational energy into the latent chemical energy of NO^+. In the suborbital flight range, the maximum molar concentration of NO^+ so produced is below 0.1%. Because of the relatively low energy involved (2.8 eV), the magnitude of the energy so transferred is correspondingly small compared with the total energy of the flow. The slight decrease in the translational temperature due to the NO^+ formation has a relatively small effect on the chemical reaction rates in the two-temperature model used because the translational temperature appears in the rate coefficient expressions under a square root in the model.[3,14,15] The electrons in such a small concentration do not affect the chemical reactions producing N, O, or NO. (The effect of electronic excitation usually associated with free electrons is accounted for in the two-temperature model by assuming that the electronic excitation is in equilibrium with the vibrational temperature.) Therefore, we simplify the two-temperature model by ignoring ionization processes altogether and assuming that air consists of five neutral species, O, N, NO, O_2, and N_2.

Global conservation of mass dictates that the sum of the densities of the five species equals the global density ρ. In addition, we assume that the elemental ratio between oxygen and nitrogen is conserved. This assumption would be rigorously true if the flow were inviscid. Even in a viscous flow, it would be true if the diffusion coefficients of the five species are such that the net rates of elemental diffusion of the nitrogen and oxygen are the same. The diffusion coefficients are known to be approximately the same between the two atomic species and among the three molecular species,[16] and, therefore, the assumption of elemental conservation is believed to be appropriate. Using these two relations, the density and number density of the five species are determined from the global density ρ and the densities of O, N, and NO.

An atom contains energy in the form of translational motion and electronic excitation. In a molecule, energy is contained also in the form of rotational and vibrational excitation. In general, it is not possible to assign any fixed amount of energy into any single mode independent of the amounts of energy contained in other modes because there can be coupling of modes.[17] For instance, the energy content in the rotational mode changes as the vibrational mode becomes excited and vice versa. Computing the flow accounting for this phenomenon is as yet not possible. For this reason, the conventional mode-separable energy assumption is used. According to this assumption, energy contained in one mode is unaffected by those contained in the other modes. This assumption is believed to be valid approximately at temperatures up to about 10,000 K.

Vibrational Model

At translational temperatures below about 5000 K, the vibrational relaxation times have been measured in the past for the following six collision pairs: 1) N_2-N_2,[18] 2) O_2-O_2,[18] 3) NO-NO,[19] 4) O_2-O,[20] 5) N_2-O,[21] and 6) N_2-NO.[22] Millikan and White[18] show that, for most of these collision pairs, the vibrational relaxation time can be expressed by

$$\text{vibrational relaxation time} = \exp(AT^{-1/3} - B)/p_c \equiv \tau_L\ \text{s} \tag{1}$$

where p_c is the partial pressure of the colliding particles in atmospheres. The values of A and B used in the present work are listed in Table 1.

The average vibrational energy of a molecule i, ϵ_i, where i = 1, 2, and 3, designated by NO, O_2, and N_2, respectively, is expressed by the harmonic oscillator model. At temperatures above about 5000 K, the rate of vibrational relaxation w_{ij} is reduced by two phenomena: the collision limiting of the vibrational relaxation times, and diffusive nature of the vibrational relaxation phenomenon. The collision-limiting phenomenon results from the fact that the vibrational relaxation time cannot be shorter than the average time of collisions among particles and is accounted for by replacing the Landau-Teller vibrational relaxation time τ_L with the effective relaxation time τ given by[3,14,15]

$$\tau = \tau_L + \tau_c \tag{2}$$

where τ_c is the average collision time. The expression for τ_c is taken from Ref. 3. The diffusive nature of the vibrational relaxation is accounted for by writing the vibrational relaxation rate in the form[3,14,15]:

$$w_{ij} = \frac{\epsilon_{viE} - \epsilon_{vi}}{\tau_{Lij} + \tau_c}\left|\frac{T_s - T_v}{T_s - T_{vs}}\right|^{s-1} \tag{3}$$

Here, T_s and T_{vs} are the translational-rotational and vibrational-electronic temperatures immediately behind the shock wave, respectively. The quantity s is given by[14,15]

$$s = 3.5\exp(-T_s/5000)$$

The quantities T_s and s are assumed to be constant for a constant j (the spatial index normal to the body).

Table 1 Vibrational relaxation time parameters A and B

Excited colliding Molecule	Species	A	B
NO	O	40	21.0
NO	N	120	21.5
NO	NO	40	20.0
NO	O_2	120	21.5
NO	N_2	120	21.5
O_2	O	40	21.0
O_2	N	60	19.0
O_2	NO	120	21.5
O_2	O_2	120	21.5
O_2	N_2	160	23.0
N_2	O	60	19.0
N_2	N	160	23.0
N_2	NO	160	23.0
N_2	O_2	160	23.0
N_2	N_2	220	25.0

The rate of increase of vibrational energy per unit volume of molecule i by collisions of all three species, W_i, is the sum of $n_i w_{ij}$ over j, where n_i is the number density of molecule i, minus the rate of removal of vibrational energy by dissociation[3,14,15]

$$W_i = \sum_j n_i w_{ij} - \bar{\epsilon}_i \left(\frac{\partial n_i}{\partial t} \right)_r$$

where $\bar{\epsilon}_i$ is the average vibrational energy removed in the dissociation of molecule i, and $(\partial n_i/\partial t)_r$ signifies the net production (production minus removal) rate of species n_i by the thermochemical processes. Following Refs. 3, 14, and 15, $\bar{\epsilon}_i$ is taken to be 80% of the dissociation energy of molecule i.

As can be deduced from the $\boldsymbol{A}$ and $\boldsymbol{B}$ values given in Table 1, the vibrational relaxation times differ greatly among various collision pairs at temperatures below about 5000 K. At higher temperatures, the relaxation times are determined mostly by the elastic collision time τ_c, which is common to all collision pairs. Therefore, in the region immediately behind the shock wave where temperature is very high, vibrational excitation of N_2 and O_2 tends to occur at nearly the same rate. In the region away from the shock wave where the temperature is relatively low but NO exists in a substantial concentration, the vibration-to-vibration energy transfers between N_2 and NO and between O_2 and NO tend to bring the vibrational temperatures of the three molecules together. This gives the justification for the two-temperature model used.

Electronic Excitation Model

In a flow where the vibrational-electronic temperature is of the order of 10,000 K or less, only those electronic states that are within about 2 eV above the ground state become significantly excited. Out of the five species under consideration, only three species, O, N, and O_2, contain electronic states within this energy range. Only these states are included in the calculation of the electronic excitation energy. We express the average electronic excitation energy per particle for species by ϵ_{ei} (see, e.g., Ref. 23, for the expression for ϵ_{ei}). The rate of change of electronic excitation energy of species i is given by

$$W_e = \sum_i \epsilon_{ei} n_i \left(\frac{\partial n_i}{\partial t} \right)_r \tag{4}$$

where $(\partial n_i/\partial t)_r$ signifies the rate of change of the number density of the species n_i by the thermochemical phenomena.

Chemical Reaction Model

The rates of reactions in un-ionized air have been measured by many investigators in the past at temperatures below about 5000 K (see, e.g., Refs. 24–26). At the two-temperature environment where T_v is significantly different from T, the chemical reaction rates are affected by T_v as well as T.[27] Following Refs. 3, 14, and 15, the rate coefficients are assumed to be a function of an average temperature T_a, which is a geometrical average between T and T_v

$$T_a = \sqrt{T_v T} \tag{5}$$

It is customary to express a rate coefficient of an endothermic reaction, referred to commonly as a forward rate k_f, in terms of the rate constant C and the pre-exponential power n in the form

$$k_f = CT^n \exp(-T_d/T)$$

where T_d is the characteristic temperature of reaction (reaction energy divided by the Boltzmann constant). According to the two-temperature model, T must be replaced by T_a:

$$k_f = CT_a^n \exp(-T_d/T_a) \tag{6}$$

The rate parameters C and n used in the present work are summarized in Table 2.

The reverse (exothermic) rates are calculated from the forward rates using the assumption that the two rates are related by the equilibrium constant evaluated at T_a, that is,

$$k_r = k_f/K_e(T_a)$$

The equilibrium constant K_e is calculated through the detailed calculation using the atomic and molecular constants and is expressed in the form[14]

$$K_e = \exp[a_1 z + a_2 + a_3 \ell n(1/z) + a_4/z + a_4/z^2] \tag{7}$$

where $z = T_a/10{,}000$. The numerical values of a_i are given in Table 3.

For the purpose of comparison, calculations have been made also with these reaction rate parameters altered. The constant C in Eq. (6) and the vibrational relaxation rates $1/\tau_L$ and $1/\tau_c$ are multiplied by 10^{-3}, 10^{-2}, 0.03, 0.1, 0.3, 3, 10, 30, and 100 for all reactions in Table 2 for this purpose. By multiplying C and the two $1/\tau$ by 100, we are forcing the flow to be nearly in thermal and chemical equilibrium. This case will be referred to hereafter as the equilibrium case. In addition, we calculated the cases where the C values are varied while keeping the $1/\tau$ values at 100 times those in Table 1. In these cases, the vibrational-electronic temperature T_v becomes nearly equal to the translational-rotational temperature T, and the gas properties will resemble those of the thermal-equilibrium (i.e., one-temperature) flow. These cases will be called the one-temperature nonequilibrium cases. The cases where the rate parameters are multiplied by 10^{-3} will be called the frozen-flow cases.

In addition, calculations have been made for the perfect gas with a γ value varying between 1.15 and 1.4 using the perfect-gas code CENS2D mentioned earlier. All of these calculated cases are summarized in Table 4.

Method of Computation

Computational Fluid Dynamics Equations

The computational fluid dynamics (CFD) equations for the finite rate chemically reacting flows are well known. In a two-dimensional flow, they can be written in the Cartesian coordinates (x,y) in the form

$$\frac{\partial Q}{\partial t} + \frac{\partial}{\partial x}(F - F_v) + \frac{\partial}{\partial y}(G - G_v) = S$$

The Q vector in the present work is

$$Q = \begin{pmatrix} \rho \\ \rho u \\ \rho v \\ E \\ E_v + E_e \\ \rho_1 \\ \rho_2 \\ \rho_3 \end{pmatrix} \tag{8}$$

Here, E is the internal energy, and ρ_1, ρ_2, and ρ_3 are the densities of the species O, N, and NO, respectively. The corresponding fluxes F, G, F_v, and G_v are well known and, therefore, are not written here (see Ref. 28). In evaluating the viscous fluxes F_v and G_v, the viscous tensors are evaluated in both x and y directions; that is, a full Navier-Stokes evaluation is made. The source production term is given by

Table 2 Reaction rate parameters in Eq. (6)

No.	Reaction	C, m^2/mole · s	n	T_d, K	Reference
1	$O_2 + O_2 \rightarrow O + O + O_2$	2.0×10^{15}	−1.5	59,500	24
2	$O_2 + O \rightarrow O + O + O$	1.0×10^{16}	−1.5	59,500	24
3	$O_2 + N_2 \rightarrow O + O + N_2$	2.0×10^{15}	−1.5	59,500	24
4	$O_2 + N \rightarrow O + O + N$	1.0×10^{16}	−1.5	59,500	Est
5	$O_2 + NO \rightarrow O + O + NO$	2.0×10^{15}	−1.5	59,500	Est
6	$N_2 + O \rightarrow NO + N$	1.8×10^{8}	0.0	76,000	25
7	$NO + O \rightarrow O_2 + N$	2.2×10^{3}	1.0	19,000	26
8	$N_2 + O \rightarrow N + N + O$	3.0×10^{16}	−1.6	113,200	Est
9	$N_2 + N \rightarrow N + N + N$	3.0×10^{16}	−1.6	113,200	24
10	$N_2 + NO \rightarrow N + N + NO$	7.0×10^{15}	−1.6	113,200	Est
11	$N_2 + O_2 \rightarrow N + N + O_2$	7.0×10^{15}	−1.6	113,200	Est
12	$N_2 + N_2 \rightarrow N + N + N_2$	7.0×10^{15}	−1.6	113,200	24

Table 3 Coefficients a_i in Eq. (7)

No.	a_1	a_2	a_3	a_4	a_5
1–5	0.55388	16.27551	1.77630	−6.5720	0.031445
6	0.97646	0.89043	0.74572	−3.9642	0.007123
7	0.004815	−1.7443	−1.2227	−0.95824	−0.045545
8–12	1.53510	15.4216	1.2993	−11.4940	−0.006980

Table 4 Calculated cases and results

Designation	Rate parameters	a/a, deg	C_L	C_D	C_m	x_{mc}, m
Std-1	×1	0	0	1.570	0	n/a
Std-2	×1	10	−0.206	1.532	−0.04016	1.328
Std-3	×1	20	−0.384	1.415	−0.07679	1.318
Std-4	×1	30	−0.505	1.228	−0.10690	1.298
Froz-1	$\times 10^{-3}$	0	0	1.521	0	n/a
Froz-2	$\times 10^{-3}$	10	−0.207	1.486	−0.03365	1.318
Froz-3	$\times 10^{-3}$	20	−0.394	1.392	−0.06575	1.313
Froz-4	$\times 10^{-3}$	30	−0.534	1.236	−0.09390	1.297
Equil	×100	20	−0.383	1.440	−0.08272	1.318
1-Ta	×1	20	−0.387	1.433	−0.07864	1.315
1-Tb	×0.1	20	−0.385	1.392	−0.07150	1.317
Slow-1	×0.01	20	−0.391	1.394	−0.06808	1.314
Slow-2	×0.03	20	−0.387	1.389	−0.06915	1.316
Slow-3	×0.1	20	−0.385	1.392	−0.07158	1.317
Slow-4	×0.3	20	−0.383	1.400	−0.07407	1.317
Fast-1	×3	20	−0.384	1.428	−0.07941	1.316
Fast-2	×10	20	−0.384	1.433	−0.08084	1.317
Fast-3	×30	20	−0.383	1.438	−0.08224	1.317
Perfect-1	$\gamma = 1.15$	20	−0.398	1.466	−0.07748	1.302
Perfect-2	$\gamma = 1.20$	20	−0.401	1.451	−0.07278	1.303
Perfect-3	$\gamma = 1.30$	20	−0.400	1.421	−0.06680	1.303
Perfect-4	$\gamma = 1.40$	20	−0.497	1.398	−0.06425	1.304

$$S = \begin{pmatrix} 0 \\ 0 \\ 0 \\ 0 \\ W_v + W_e \\ W_1 \\ W_2 \\ W_3 \end{pmatrix} \tag{9}$$

This system of equations is then converted into a curvilinear coordinate system in ξ and η. Let A and B be the Jacobian matrices of the inviscid flux vectors in the ξ-η coordinates, D_ξ and D_η the difference operators that approximate $\partial/\partial\xi$ and $\partial/\partial\eta$, and δQ the correction. Then, the unfactored linearized implicit scheme can be written as

$$[I + \beta\Delta t(D_\xi A + D_\eta B - H)]\delta Q$$

$$= -\Delta t[D_\xi(F - F_v) + D_\eta(G - G_v) + S]$$

where $H = \partial S/\partial Q$, and β is 1 or $^1/_2$ depending on the order of accuracy or stability chosen. The first-order (in time) accurate lower-upper symmetric Gauss-Seidel (LU-SGS) implicit factorization scheme[11,12] can be written as

$$LD^{-1}U\delta Q = -\Delta t \times R \tag{10}$$

where

$$L = I + \beta\Delta t(D_\xi^- A^+ + D_\eta^- B^+ - A^- - B^- - H)$$

$$D = I + \beta\Delta t(A^+ + B^+ - A^- - B^-)$$

$$U = I + \beta\Delta t(D_\xi^+ A^- + D_\eta^+ B^- + A^+ + B^+)$$

and R is the right-hand-side (RHS) residual:

$$R = D_\xi(F - F_v) + D_\eta(G - G_v) + S \tag{11}$$

Here, D_ξ^- and D_η^- are the backward difference operators and D_ξ^+ and D_η^+ are the forward difference operators. We use the central difference operators to the unsplit inviscid fluxes on the RHS and the approximate Jacobian matrices on the left-hand side (LHS) to obtain a hybrid LU-SGS scheme. By setting Δt to infinity, we obtain a Newton iteration form. The Jacobian matrices are approximately constructed to obtain diagonal dominance. Designating the matrices with non-negative and nonpositive eigenvalues with the superscripts "+" and "−", respectively, the resulting matrices have a form

$$A^\pm = {^1/_2}[A \pm \rho(A)I]$$

where

$$\rho(A) = \kappa \max[|\lambda(A)|] \tag{12}$$

Here, $\lambda(A)$ represents the eigenvalues of the Jacobian matrix A, and κ is an arbitrary constant that is ≥ 1.

To suppress the tendency for odd and even point decoupling, and to prevent unphysical oscillations near discontinuities, a flux-limited dissipation model is incorporated in the present calculation.[11] The details are given in Ref. 28.

The flow is assumed to be laminar throughout. The viscosity is assumed to be proportional to the 0.72 power of T. The thermal conductivity is calculated from the viscosity value assuming that the frozen Prandtl number is 0.72. The species-averaged diffusion coefficient[13] is used instead of the rigorous multicomponent diffusion coefficient. The species-averaged diffusion coefficient is deduced from the viscosity assuming the frozen Schmidt number to be 0.72. The conductivity of the vibrational-electronic energy is calculated from the diffusion coefficients of the molecular species.

Flowfield

The computing technique developed in the present work is applied to solve the two-dimensional flowfield over a blunt body whose profile is the same as that of the forebody portion of the Apollo Command Module. The computing grid is generated algebraically. In the η direction, the spacing at the wall is 10% of that of the average value. The body profile is symmetric with respect to the horizontal axis, $y = 0$, and has an overall radius of 1.955 m. The stagnation region of the body is a circle of 4.694-m radius. The rest of the forebody is formed by an ellipse whose major and minor axes are 1.627 and 0.564 m, respectively. The afterbody is taken for this calculation to be a straight line starting at $x = 0.6930$ m. The forebody is defined as the region $x \le 0.6930$ m. The number of the computing nodes are taken to be 69 in the streamwise (ξ) and 79 in the crosswise (η) directions, to a total of 5451 computing points. Lift, drag, and pitching moment are calculated from the pressure distribution over the forebody region, neglecting viscous wall shear. Viscous shear is neglected because it contributes negligibly to the overall forces and moments in the environment of concern. The contribution of the base region is neglected for the same reason. Moreover, there is a serious doubt as to whether this code, or any other code for that matter, can calculate the base flow accurately. The pitching moment is calculated around the reference point $x = 0.6930$, $y = 0$ m. The body diameter d is taken to be the reference length in the calculation of these coefficients. The wall is assumed to be noncatalytic to all chemical reactions. The surface of the Apollo vehicle was ablating and was neither a catalytic nor a noncatalytic wall. The assumption of the noncatalytic wall was used here merely for simplificaton. Since the wall catalyticity has virtually no connection to the pressure distribution, the assumption is inconsequential. Both the translational-rotational temperature T and the vibrational-electronic temperature T_v are assumed to be 1500 K at the wall.

A uniform supersonic flow at an angle of attack α in the range from 0 to 30 deg is assumed to flow over this body. The calculation is initiated with the uniform flow as the starting solution. The density, velocity, and temperature of the freestream flow are taken to be 2.164×10^{-5} kg/m^3, 6958 m/s, and 300 K, respectively. The density is that at an altitude of 78 km. The Mach number of this flow is 20. The Reynolds number is 1×10^4/m in the freestream (based on the viscosity of the freestream flow). The angle of attack is defined in the computation by the conventional method; that is, it is the angle between the direction of the wind vector (oncoming flow) and the horizontal axis. The generated lift is negative, that is, it is pointed downward. The angle of attack defined in computation is related to that in the Apollo convention (Fig. 1a) by

$$\text{computational } a/a = 180\text{ deg} - \text{Apollo } a/a \tag{13}$$

Results

General Features of the Solutions

The computation was made in a CRAY Y-MP computer. Each iteration required 0.273 s with the CENS2H code. The per-point computing speed is 5.0×10^{-5} s/iteration step/node point. With the perfect-gas code, CENS2D, each iteration step required 0.111 s, or 41% of the reacting case.

In Fig. 3, the convergence histories for the standard two-temperature case (designated Std-3 in Table 4), the one-temperature case (designated 1-Ta), and the equilibrium case are compared with that of the frozen-flow case. In the figure, the abscissa are the iteration numbers and the ordinates are the root-mean-square of the residual R given by Eq. (11). The figure shows that the residue decreases by nearly three orders of magnitude within 5000 iterations.

In Fig. 4, the convergence history of the calculated values of the pitching moment coefficient C_m around the reference point is compared among the same four cases. As seen here, pitching moment reaches an asymptotic limiting value at the point where the residual has fallen by three orders of magnitude.

Figures 5a and 5b show the calculated T and T_v for the standard two-temperature nonequilibrium case. The peak value of T_v is below 8500 K, whereas the peak value for T is nearly

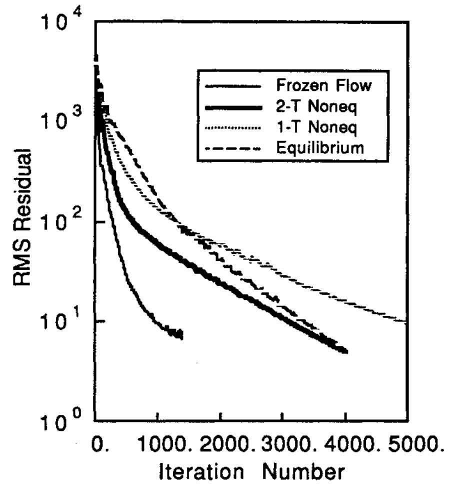

Fig. 3 Convergence history showing the root-mean-square residual against the iteration number for the one- and two-temperature nonequilibrium flows, frozen flow, and equilibrium flow.

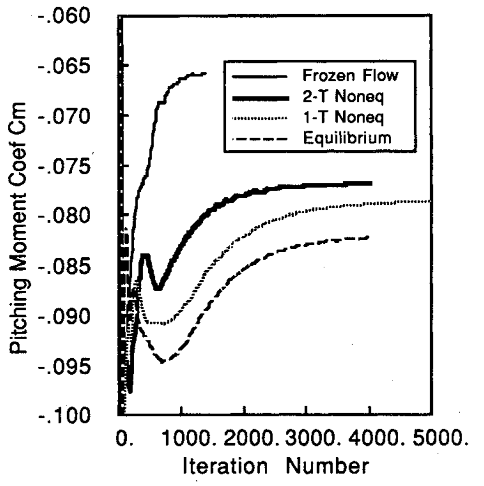

Fig. 4 Convergence history of the pitching moment coefficient C_m shown against the iteration number for the one- and two-temperature nonequilibrium flows, frozen flow, and equilibrium flow.

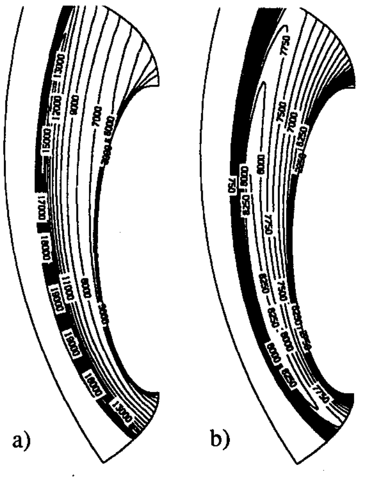

Fig. 5 Flow temperatures, in degrees K, in the standard two-temperature nonequilibrium case (Std-3 in Table 2): a) translational-rotational temperature; b) vibrational-electronic temperature.

20,000 K. Thus, a strong two-temperature thermal nonequilibrium environment is seen to exist for the calculated case.

In Figs. 6a and 6b, the calculated mass percentages of nitrogen and nitric oxide are shown for the standard two-temperature nonequilibrium case, respectively. As shown here, the flow is significant in chemical nonequilibrium throughout the shock layer.

In Figs. 7a and 7b, the shapes of the shock waves are shown for the frozen flow, one- and two-temperature nonequilibrium flows, and the equilibrium flow. In Fig. 7a, the two nonequilibrium cases are calculated with the standard rate coefficients (Std-3 and 1-Ta). In Fig. 7b, they are calculated with the rates 1/10 those of the standard values (Slow-2 and 1-Tb). As seen here, the shock shapes are, in general, discernibly different among the four cases. For the cases shown in Fig. 7b, the one-temperature nonequilibrium model results in a shock standoff distance substantially smaller than that obtained by the two-temperature nonequilibrium model. Though not shown here, the shock shape for the perfect-gas case with $\gamma = 1.2$ is nearly the same as for the standard two-temperature nonequilibrium case. (The shock standoff distance for $\gamma = 1.2$ is very slightly smaller than for the two-temperature nonequilibrium case.)

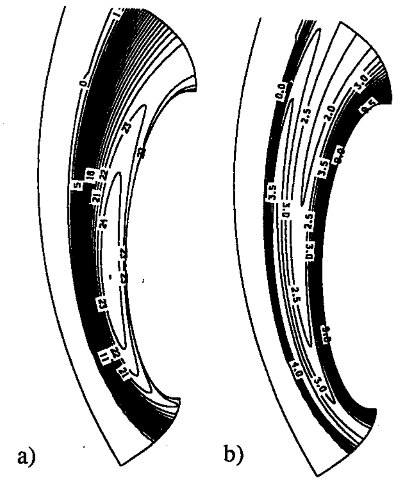

Fig. 6 Mass percentages in the two-temperature nonequilibrium case: a) atomic nitrogen; b) nitric oxide.

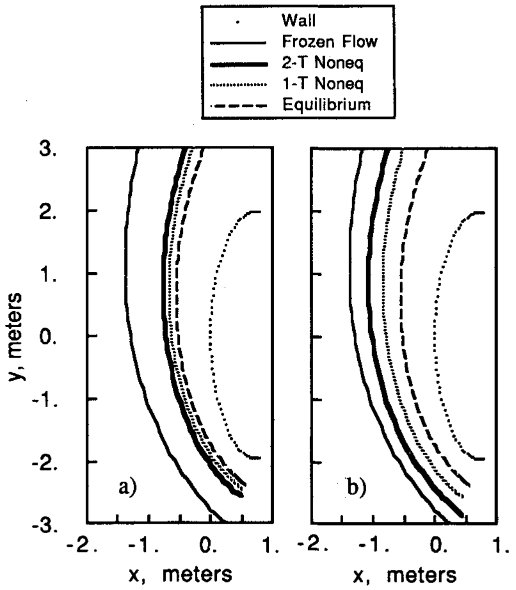

Fig. 7 Shock shapes for two- and one-temperature nonequilibrium flows, frozen flow, and equilibrium flow: a) standard rate coefficients (Std-3 and 1-Ta); b) rate coefficients 1/10 the standard values (Slow-2 and 1-Tb). (Though not shown, the perfect gas with $\gamma = 1.2$ results in nearly the same shock shape as the standard two-temperature case.)

In Fig. 8, the pressure coefficient C_p is compared among several solutions in the range $C_p \geq 1.5$. In the figure, the abscissa are the distance along the wall measured from the lower (windward side) frustrum edge ($x = 0.6930$, $y = -1.955$ m). The figure shows that pressure is the greatest for the equilibrium case. The peak pressure for the case of $\gamma = 1.2$ is nearly the same as that of the standard two-temperature nonequilibrium case. However, the pressure difference between the $\gamma = 1.2$ and the nonequilibrium cases is greater at larger distances. This fact is bound to impact the relative magnitudes of the trim angles between the two solutions, as will become apparent later.

In Fig. 9, a similar comparison is made among the three solutions of the two-temperature reaction model with different rate coefficients, the frozen-flow case, and the one-temperature nonequilibrium case. As seen here, there is a monotonic deviation from the frozen-flow solution as the rate coefficients are increased. The one-temperature model results in a pressure distribution substantially different from that for the two-temperature model for the same given rate parameters; the one-temperature solution results in nearly the same pressure distribution as the two-temperature solution with three times the rate constants. It is expected that the one-temperature model assumes an instant equilibration of vibrational temperature with

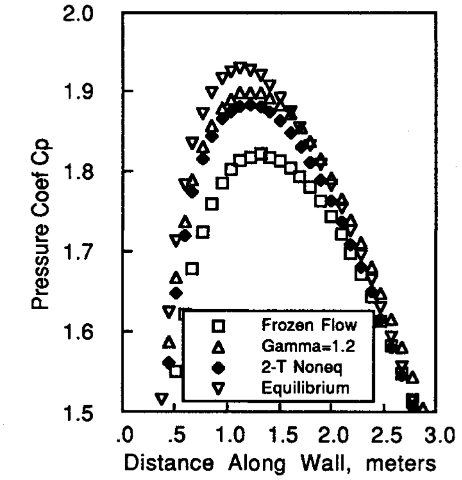

Fig. 8 Pressure coefficients along the wall for the frozen flow, the perfect gas with $\gamma = C_p/C_v = 1.2$, the two-temperature nonequilibrium flow, and the equilibrium flow.

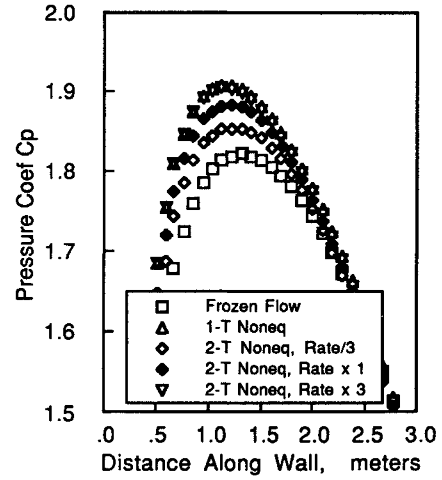

Fig. 9 Pressure coefficients along the wall for the frozen flow, one-temperature nonequilibrium flow, and the two-temperature nonequilibrium flow with different rate constants.

the translational temperature and, therefore, the vibrational temperatures in the one-temperature model are always higher than those of the two-temperature model. The higher vibrational temperature leads to the high chemical reaction rates.

Trim Angle of Attack

The calculated values of the pitching moment coefficient C_m around the reference point are listed in Table 4. As the table shows, C_m is approximately proportional to the angle of attack. The pitching moment derivative $dC_m/d\alpha$ is about -0.2 between the angles of attack of 10 and 30 deg, signifying that the body is statically stable in this range of angle of attack (provided the c.g. is placed at the reference point).

From the pitching moment coefficent C_m and the lift and drag coefficients C_L and C_D, one can construct the resultant force line, the direction and location of which represent those of the resultant force vector. At a finite angle of attack, this force line intersects the axis of the body. This intersection point has an important meaning in the stability of the vehicle and was named a metacenter.[29] The locations of the metacenter, measured from the stagnation point x_{mc} are also listed in Table 4. As seen in the table, x_{mc} is relatively insensitive to angle of attack.

Assuming that $dC_m/d\alpha$ and x_{mc} are independent of α, one can determine the trim angle of attack α_t for a given c.g. location. Denoting the coordinates of the c.g. by $\bar{x}$ and e (see Fig. 1), the trim angle of attack can be shown to be

$$\alpha_t = \alpha \frac{\theta_2}{\theta_1}$$

where

$$\theta_1 = \alpha + \tan^{-1}\left(\frac{C_L}{C_D}\right), \quad \theta_2 = \tan^{-1}\left(\frac{e}{x_{mc} - \bar{x}}\right)$$

Thus, the trim angle is a function of the c.g. location. For the flight AS-202 of the Apollo vehicle (see Fig. 1), the c.g. location is calculated to be $\bar{x} = 1.077$ m and $e = 0.135$ m. However, these values cannot be used directly in the present work because, unlike the Apollo vehicle, which was axisymmetric, the present calculation is made for a two-dimensional body. Therefore, calculations are made assuming an arbitrary fixed $\bar{x}$ value of 1 m, and the e value varying arbitrarily.

The trim angles of attack α_t calculated by this method are plotted in Fig. 10 for $e = 0.030$ and 0.035 m. As Fig. 10 shows, the trim angle of attack decreases as the rate constant increases. Between the largest and the smallest rate coefficients shown in the figure, there is a difference of more than 5 deg in the trim angle. The two curves are identical and are only displaced vertically. Thus, the magnitude of the shift in trim angle is independent of the e value chosen, at least within the calculated range. Since the angle of attack defined here is the opposite of that in Apollo [see Eq. (13)], the trend seen in this figure is the same as that during the Apollo flight shown in Fig. 2. The calculated extent of the shift in the trim angle is also of the same order as that observed during the Apollo flight. Interestingly, the trim angles for the one-temperature nonequilibrium model are nearly identical to those for the two-temperature model. This is surprising, considering that the shock shapes are sustantially different between the two models (see Fig. 7).

In Fig. 11, the trim angles calculated by the perfect-gas model are shown as a function of γ. For $\gamma = 1.4$, the trim angle is slightly larger than that of the frozen flow (rate multiplied by 10^{-3}) shown in Fig. 10, as expected. As γ is decreased, the trim angle decreases. For the $\gamma = 1.2$ case, which approximately reproduces the shock standoff distance (Fig. 7) and the peak pressure of the two-temperature nonequilibrium case (see Fig. 8), the trim angle is nearly 3 deg greater than that for the nonequilibrium case. Thus, one sees that the trim angle in a nonequilibrium flow cannot be reproduced by a perfect-gas calculation with an effective γ, even when that correctly reproduces the shock standoff distance. This phenomenon is attributable to the fact that the pressure difference between the $\gamma = 1.2$ and the nonequilibrium cases is larger at larger distances along the wall surface, as seen in Fig. 8.

Discussion

The present results indicate that the computing technique developed for the two-temperature reacting flow in the present work converges satisfactorily for a typical problem in two dimensions. The technique can be applied to computing pitching moments and trim angles to obtain results that are sufficiently consistent and reproducible for the purpose of comparing with the experimental data. This provides an encouragement to extend the technique to the three-dimensional flowfields.

The present results show also that the pitching moments and trim angles of attack are indeed affected by chemical reactions. The direction and the extent of the difference in the trim angle of attack between the perfect-gas and the reacting-gas cases calculated in the present work are the same and of the same order as those observed during the Apollo entry flights. This confirms the assessment by the earlier investigators[4-8] that the trim shift was caused by the high-temperature real-gas effects. The one-temperature and the two-temperature nonequilibrium models give nearly the same trim angles. The perfect-gas, constant-γ solutions that reproduce the shock standoff distances

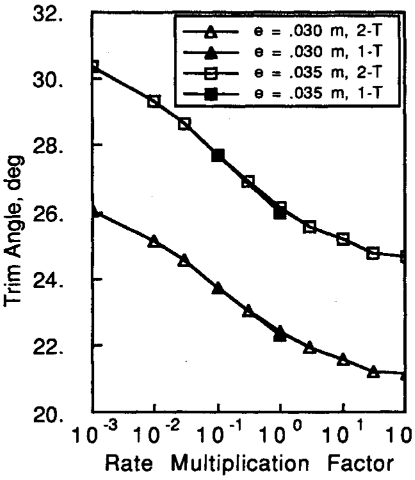

Fig. 10 Trim angle of attack calculated by the one- and two-temperature nonequilibrium models with different reaction rate constants. (The rate multiplication factor of 1 designates the rate constant values given in Table 2.)

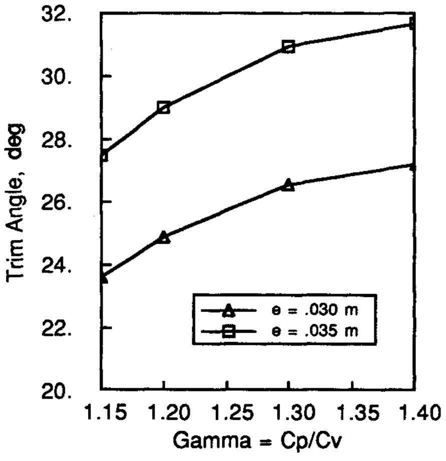

Fig. 11 Trim angle of attack calculated by the perfect-gas model with different γ.

of the nonequilibrium flow do not reproduce the trim angles of the nonequilibrium flow.

Conclusions

A thermochemical nonequilibrium flow expected at suborbital hypersonic flight speeds over a blunt body can be calculated using a technique based on the two-temperature model and lower-upper symmetric Gauss-Seidel sweeping technique. The technique converges and yields useful results for two-dimensional flows. When this technique is applied to a two-dimensional flow over an Apollo-shaped blunt body, the trim angle of attack is seen to decrease as the chemical reaction rates are increased. The calculated extent of the shift in the trim angle is of the same order as those observed during the flights of the Apollo vehicles. The one- and the two-temperature nonequilibrium models yield the same trim angles, but the perfect-gas, constant-γ solutions do not give the same trim angles as the nonequilibrium solutions even when they yield the same shock standoff distances.

References

[1]Rakich, J. V., Bailey, H. E., and Park, C., "Computation of Nonequilibrium, Supersonic Three-Dimensional Inviscid Flow over Blunt-Nosed Bodies," *AIAA Journal*, Vol. 21, No. 6, 1983, pp. 834–841.

[2]Candler, G. V., and MacCormack, R. W., "The Computation of Hypersonic Ionized Flows in Chemical and Thermal Nonequilibrium," AIAA Paper 88-0511, Jan. 1988.

[3]Park, C., "Assessment of Two-Temperature Kinetic Model for Ionizing Air," *Journal of Thermophysics and Heat Transfer*, Vol. 3, No. 3, 1989, pp. 233–244.

[4]Crowder, R. S., and Moote, J. D., "Apollo Entry Aerodynamics," *Journal of Spacecraft and Rockets*, Vol. 6, No. 3, 1969, pp. 302–307.

[5]Hillje, E. R., and Savage, R., "Status of Aerodynamic Characteristics of the Apollo Entry Configuration," AIAA Paper 68-1143, Dec. 1968.

[6]Romere, P. O., and Whitnah, A. M., "Space Shuttle Entry Longitudinal Aerodynamic Comparisons of Flights 1–4 With Preflight Predictions," *Shuttle Performance: Lessons Learned*, compiled by J. P. Arrington and J. J. Jones, NASA CP 2283, March 1983, pp. 283–307.

[7]Mosley, W. C., Jr., and Martino, J. C., "Apollo Wind Tunnel Testing Program—Historical Development of General Configuration," NASA TN D-3748, Dec. 1966.

[8]Griffith, B. J., Maus, J. R., and Best, J. T., "Explanation of the Hypersonic Longitudinal Stability Problem," *Shuttle Performance: Lessons Learned*, compiled by J. P. Arrington and J. J. Jones, NASA CP 2283, March 1983, pp. 283–307.

[9]Boylan, D. E., and Griffith, B. J., "Simulation of the Apollo Command Module Aerodynamics at Re-Entry Altitudes," *Proceedings of the 3rd National Conference on Aerospace Meteorology*, American Meteorological Society, New Orleans, LA, May 1968, pp. 370–378.

[10]De Rose, C. E., "Trim Attitude, Lift, and Drag of the Apollo Command Module with Offset Center-of-Gravity Positions at Mach Numbers to 29," NASA TN D-5276, June 1969.

[11]Yoon, S., and Kwak, D., "Artificial Dissipation Models for Hypersonic External Flow," AIAA Paper 88-3708, July 1988.

[12]Yoon, S., and Jameson, A., "An LU-SSOR Scheme for the Euler and Navier-Stokes Equations," AIAA Paper 87-0600, Jan. 1987.

[13]Shuen, J. S., and Yoon, S., "Numerical Study of Chemically Reacting Flows Using an LU Scheme," AIAA Paper 88-0436, Jan. 1988.

[14]Park, C., "Convergence of Computation of Chemically Reacting Flows," *Thermophysical Aspects of Re-Entry Flows*, edited by J. N. Moss and C. D. Scott, Vol. 103, Progress in Astronautics and Aeronautics, AIAA, New York, 1986, pp. 478–513.

[15]Park, C., "Assessment of Two-Temperature Kinetic Model for Dissociating and Weakly-Ionizing Nitrogen," *Journal of Thermophysics and Heat Transfer*, Vol. 2, No. 1, 1988, pp. 8–16.

[16]Yos, J. M., "Transport Properties of Nitrogen, Hydrogen, Oxygen, and Air to 30,000 K," AVCO Corporation, TM RAD TM-63-7, Wilmington, MA, March 1963.

[17]Jaffe, R. L., "The Calculation of High-Temperature Equilibrium and Nonequilibrium Specific Heat Data for N_2, O_2, and NO," AIAA Paper 87-1633, June 1987.

[18] Millikan, R. C., and White, D. R., "Systematics of Vibrational Relaxation," *Journal of Chemical Physics*, Vol. 39, No. 12, 1963, pp. 3209–3213.

[19]Wray, K., "Shock-Tube Study of the Vibrational Relaxation of Nitric Oxide," *Journal of Chemical Physics*, Vol. 36, No. 10, 1962, pp. 2597–2603.

[20]Kiefer, J. H., and Lutz, R. W., "The Effect of Oxygen Atoms on Vibrational Relaxation of Oxygen," *Proceedings of the 11th Symposium (International) on Combustion*, Combustion Inst., Pittsburgh, PA, 1967, pp. 67–76.

[21]Eckstrom, D. J., "Vibrational Relaxation of Shock-Heated N_2 by Atomic Oxygen Using the IR Tracer Method," *Journal of Chemical Physics*, Vol. 59, No. 6, 1973, pp. 2787–2795.

[22]Taylor, R. L., Camac, M., and Feinberg, R. M., "Measurements of Vibration-Vibration Coupling in Gas Mixtures," *Proceedings of the 11th Symposium (International) on Combustion*, Combustion Inst., Pittsburgh, PA, 1967, pp. 49–65.

[23]Lee, J. H., "Basic Governing Equations for the Flight Regimes of Aeroassisted Orbital Transfer Vehicles," *Thermal Design of Aeroassisted Orbital Transfer Vehicles*, edited by H. F. Nelson, Vol. 96, Progress in Astronautics and Aeronautics, AIAA, New York, 1985, pp. 3–53.

[24]Park, C., "Two-Temperature Interpretation of Dissociation Rate Data for N_2 and O_2," AIAA Paper 88-0458, Jan. 1988.

[25]Monat, J. P., Hanson, R. K., and Kruger, C. H., "Shock Tube Determination of the Rate Coefficient for the Reaction $N_2 + O \rightarrow NO + N$," *Proceedings of the 17th Symposium (International) on Combustion*, Combustion Inst., Pittsburgh, PA, 1978, pp. 543–552.

[26]Hanson, R. K., Flower, W. L., and Kruger, C. H., "Determination of the Rate Constant for the Reaction $O + NO \rightarrow N + O_2$," *Combustion Science and Technology*, Vol. 9, Nos. 3–4, June 1974, pp. 79–86.

[27]Park, C., "Problems of Rate Chemistry in the Flight Regimes of Aeroassisted Orbital Transfer Vehicles," *Thermal Design of Aeroassisted Orbital Transfer Vehicles*, edited by H. F. Nelson, Vol. 96, Progress in Astronautics and Aeronautics, AIAA, New York, 1985, pp. 511–537.

[28]Park, C., and Yoon, S., "Calculation of Real-Gas Effects on Blunt-Body Trim Angles," AIAA Paper 89-0685, Jan. 1989.

[29]Davies, C. V., and Park, C., "Aerodynamics of Generalized Bent Biconics for Aero-Assisted, Orbital-Transfer Vehicles," *Journal of Spacecraft and Rockets*, Vol. 22, No. 2, 1985, pp. 104–111.